

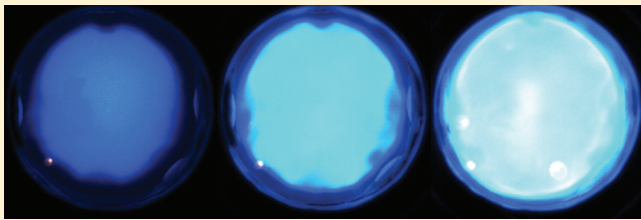
On the Chemical Kinetics of *n*-Butanol: Ignition and Speciation Studies

Darshan M.A. Karwat,^{*,†} Scott W. Wagnon,[‡] Paul D. Teini,[‡] and Margaret S. Wooldridge^{†,‡}

[†]Department of Aerospace Engineering and [‡]Department of Mechanical Engineering, University of Michigan, Ann Arbor, Michigan 48109, United States

 Supporting Information

ABSTRACT: Direct measurements of intermediates of ignition are challenging experimental objectives, yet such measurements are critical for understanding fuel decomposition and oxidation pathways. This work presents experimental results, obtained using the University of Michigan Rapid Compression Facility, of ignition delay times and intermediates formed during the ignition of *n*-butanol. Ignition delay times for stoichiometric *n*-butanol/O₂ mixtures with an inert/O₂ ratio of 5.64 were measured over a temperature range of 920–1040 K and a pressure range of 2.86–3.35 atm and were compared to those predicted by the recent reaction mechanism developed by Black et al. (*Combust. Flame* 2010, 157, 363–373). There is excellent agreement between the experimental results and model predictions for ignition delay time, within 20% over the entire temperature range tested. Further, high-speed gas sampling and gas chromatography techniques were used to acquire and analyze gas samples of intermediate species during the ignition delay of stoichiometric *n*-butanol/O₂ ($\chi(n\text{-but}) = 0.025$, $\chi(\text{O}_2) = 0.147$, $\chi(\text{N}_2) = 0.541$, $\chi(\text{Ar}) = 0.288$) mixtures at $P = 3.25$ atm and $T = 975$ K. Quantitative measurements of mole fraction time histories of methane, carbon monoxide, ethene, propene, acetaldehyde, *n*-butyraldehyde, 1-butene and *n*-butanol were compared with model predictions using the Black et al. mechanism. In general, the predicted trends for species concentrations are consistent with measurements. Sensitivity analyses and rate of production analyses were used to identify reactions important for predicting ignition delay time and the intermediate species time histories. Modifications to the mechanism by Black et al. were explored based on recent contributions to the literature on the rate constant for the key reaction, *n*-butanol+OH. The results improve the model agreement with some species; however, the comparison also indicates some reaction pathways, particularly those important to ethene formation and removal, are not well captured.



1. INTRODUCTION

Bioethanol is at present the most widely produced biofuel and is used both as an additive to petrol/gasoline and as a fuel in its own right in specially modified vehicles. There are significant concerns, ethical and environmental, about ethanol production from food stocks. Interest in butanol has therefore increased due to the variety of potential feed stock sources. Butanol has a higher lower heating value than ethanol and reduced miscibility in water as compared to ethanol.² Consequently, butanol is more attractive for application to aviation, transport, and storage as compared to ethanol, although toxic pollutants such as aldehydes and ketones, which are harmful to health, are formed as combustion byproducts from both ethanol and butanol.³

There has been much recent work studying the combustion chemistry of butanol (all four isomers), including studies of flame characteristics and propagation,^{4–7} ignition,^{1,8–11} decomposition,¹² pyrolysis,^{13,14} and elementary reaction rates.^{15,16} Most work has been performed in the high-temperature regime ($T > 900$ K); however, an early pyrolysis study investigated *n*-butanol pyrolysis at low temperatures ($T < 800$ K).¹⁴ Recent decomposition studies have further investigated the effects of adding *n*-butanol to well-studied *n*-alkanes.^{17,18}

McEnally and Pfefferle⁴ compared the kinetics of the four isomers of butanol in co-flowing methane/air flames. The authors state that although oxygenates are regarded as clean-burning fuels, the alkenes formed from the butanols can participate in hydrocarbon growth processes that lead to aromatics and soot, and during their experiments they observed the butanol-doped flames to be much more luminous than the undoped methane flame. Further, the branched isomers of butanol produced more soot precursors and benzene than did the linear isomers. They concluded that the branched nature of the fuels plays a more important role in soot formation than the presence or absence of oxygen bound in the fuel.

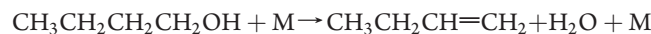
Several reaction mechanisms have also been developed in conjunction with these experimental studies. To date, ignition studies of butanol isomers have been studied predominantly in high- and low-pressure shock tubes. Heufer et al.⁹ measured ignition delay times in the range of 10–42 atm and 770–1250 K using stoichiometric fuel/oxidizer/diluent mixtures. Moss et al.⁸ conducted an experimental and kinetic modeling study of the

Received: January 27, 2011

Revised: March 18, 2011

Published: April 22, 2011

oxidation of the four isomers of butanol for $\phi = 0.25, 0.5$, and 1 , at temperatures between 1196 and 1823 K and pressures near 1 atm, with varying dilution levels. The chemical kinetic mechanism developed did not include low-temperature alkylperoxy chemical pathways. They found that *n*-butanol is the most reactive isomer, followed by *iso*-butanol, 2-butanol, and finally *tert*-butanol. Black et al.¹ conducted a similar study, in which *n*-butanol ignition experiments were performed at $\phi = 0.5, 1$, and 2 , with pressures between 1 and 8 atm, over a range of temperatures from 1100 to 1800 K. Most of the data were obtained at a dilution level of $\sim 95\%$ (argon), with one series at a dilution of 77% . The authors also developed a chemical kinetic mechanism for *n*-butanol, based on *n*-butane chemistry¹⁹ for a wide temperature (740 – 1660 K) and pressure range (1 – 34 atm). Included were simple β -scission reactions, as well as complex scission, in particular the four-centered elimination of water to form 1-butene:



Reaction path analysis carried out for $\phi = 1$, $T = 1450$ K, showed H-atom abstraction to be the principal route of consumption of *n*-butanol, in accordance with previous modeling results.^{8,20} Abstraction from the α position dominates, followed by the β , γ , and δ positions, while abstraction from the hydroxyl group is of lesser importance. At high temperatures, sensitivity analysis for $\phi = 2$ showed that small radical reactions (such as $\text{H} + \text{O}_2$) have the greatest influence on ignition delay time. The most sensitive fuel reaction is scission of the $\text{C}_\alpha-\text{C}_\beta$ bond, which increases the overall reactivity of the system. While these works have led to major developments in the detailed reaction mechanisms for *n*-butanol combustion, the effects of lower temperatures on *n*-butanol reactivity are much less well-known.

Understanding *n*-butanol combustion chemistry is vital to the successful development of renewable fuel strategies. Experiments which provide quantitative data on the reactivity and key reaction pathways of *n*-butanol are important for understanding the fundamental chemistry of this oxygenated fuel. Measurements of intermediate species concentrations during the ignition delay time provide experimental evidence of reaction pathways of fuel consumption and pollutant formation. However, quantifying these intermediates is difficult, due to the sampling and analytical methods required. To our knowledge, only two speciation studies of *n*-butanol oxidation and ignition exist in the literature. Sarathy et al.¹² studied *n*-butanol decomposition and combustion through experimental studies in a jet-stirred reactor at a mean residence time of 0.07 s, a constant pressure of 1 atm, and over a temperature range of 800 – 1300 K. Their studies included measurements of the parent fuel, methane, ethane, ethene, acetylene, propene, formaldehyde, acetaldehyde, butyraldehyde, 1-butene, carbon dioxide, and carbon monoxide as a function of different reactor temperatures. They found, at $T = 1160$ K and $\phi = 1$, the leading consumption pathways of *n*-butanol to be complex fission resulting in the formation of 1-butene and H_2O (25%) and H-atom abstraction (60%), with H atoms (29%) and OH (57%) radicals being the main contributors to H-atom abstraction.

Osswald et al.⁶ studied fuel-rich ($\phi = 1.7$), low-pressure flames of the four isomers of butanol using molecular beam mass spectrometry. The authors were able to identify 57 chemical species, including radical and isomeric species, at various heights above their porous plug burners using a combination of electron

ionization and photoionization mass spectrometry. The authors were able to characterize pollutant emissions and soot precursors from the flames of the four isomers, with fuel structure significantly influencing the concentrations of these products; high concentrations of formaldehyde and acetaldehyde were detected in *n*-butanol flames, and while *tert*-butanol flames produced low concentrations of oxygenated intermediates, they did produce higher concentrations of propargyl and benzene, both of which are soot precursors.

The objective of the current study is to provide new insights into the low-temperature combustion chemistry of *n*-butanol through ignition and speciation studies. The experimental measurements of *n*-butanol ignition delay times and intermediate species measurements are targeted to provide new data and metrics that extend our quantitative understanding of *n*-butanol combustion chemistry at conditions relevant to modern jet and internal combustion engines.

2. EXPERIMENTAL SETUP

2.1. University of Michigan Rapid Compression Facility. The University of Michigan Rapid Compression Facility (UM RCF) is a unique and powerful apparatus for fundamental studies of fuel chemistry over a broad range of thermodynamic conditions. Numerous studies of combustion chemistry have been completed using the UM RCF, including ignition studies of reference hydrocarbon fuel compounds such as *iso*-octane,^{21,22} simulated syngas mixtures of hydrogen and carbon monoxide,²³ and oxygenated hydrocarbons.²⁴ Differential laser absorption has been applied to UM RCF studies of *iso*-octane/air mixtures to provide time-resolved measurements of the hydroxyl (OH) radical.²⁵ More recent work has focused on quantitative measurements of intermediate species by gas chromatography using rapid gas sampling during UM RCF experiments of *iso*-octane/air²⁶ and methyl butanoate/air²⁷ mixtures.

The UM RCF uses a free-piston/cylinder compression process to create a chemical reactor for combustion chemistry studies. The key characteristics of the combustion kinetics are interrogated using the optical and physical access provided by the test section of the facility. The UM RCF consists of five major components as shown in Figure 1—the driver section, the driven section, the test section (or test manifold), the sabot (a free piston with a tapered nose cone that forms an interference fit with the test section), and the hydraulic globe valve system. At the start of an experiment, the sabot is located at the upstream end of the driven section. The driven section (2.74 m long, 101.2 mm inner diameter) is evacuated and then filled with a pre-prepared fuel/oxidizer/diluent mixture. The driver section (with an inner diameter of 154 mm) is charged with high-pressure gas. The driver and driven sections are separated by the fast-acting globe valve. When the valve is opened (with a typical cycle time of 100 ms), the sabot is launched down the length of the driven section compressing the test gas mixture. At the end of compression (EOC), the nose cone of the sabot seals the fuel/oxidizer/diluent mixture in the test section at specifically targeted temperatures and pressures, with the majority of the rise in temperature and pressure occurring during the last 10 ms of the stroke. Targeted temperatures and pressures are achieved by varying the compression ratio of the test section, as well as the composition of inert gases in the test mixture. At a given pressure and temperature after EOC, the fuel/oxidizer/diluent mixture in

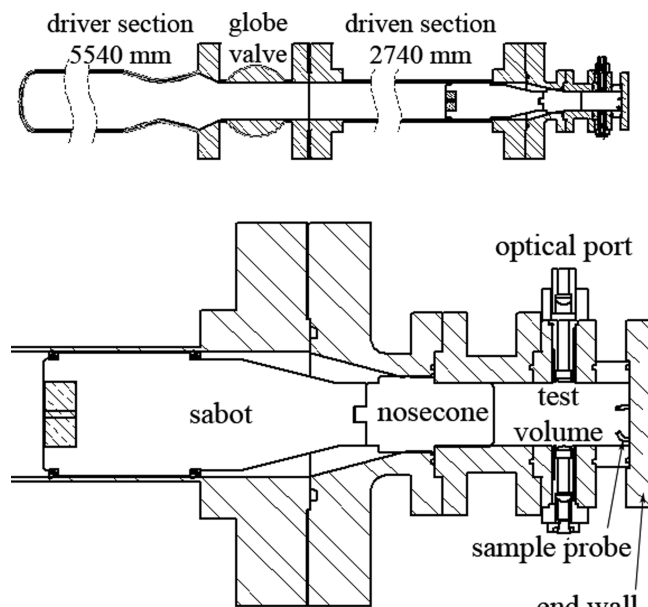


Figure 1. Top panel is a schematic of the major components of the UM RCF. The lower panel presents a detailed view of the test section showing the configuration of equipment used during high-speed gas sampling experiments. Only the probes of the gas-sampling system are shown in the schematic.

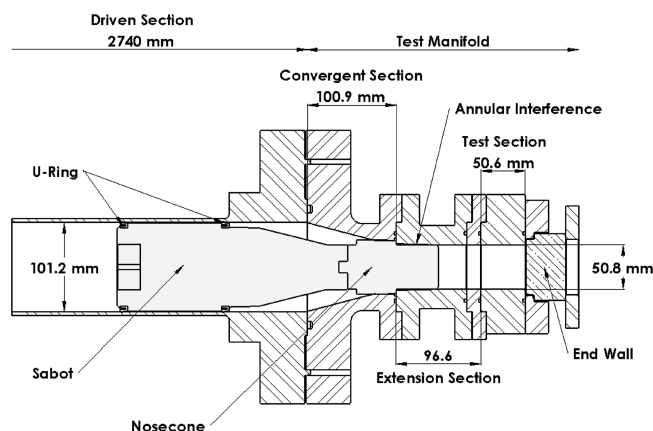


Figure 2. Schematic of the test section of the UM RCF configured for end-view imaging, including key dimensions.

the test section autoignites after a period of time that is designated the ignition delay time (τ_{ign}).

The UM RCF is designed to create uniform conditions at EOC to isolate reaction chemistry during the experiments and to minimize other interfering effects. Two important features include the geometry of the convergent section and the mixing manifold. The convergent section, the test section, and the nose cone of the sabot are designed to trap the cold boundary layer outside the test section. Figure 2 shows a schematic of these RCF components with key dimensions. The unique shape of the sabot and the geometry of the convergent section cause the core region of the test gases to be compressed into the test section, trapping the cold boundary layer gases in the shoulder region created by the body of the sabot and the convergent section. The compression of the core gases is therefore well-described as an isentropic process, and characterization studies show less than 5%

difference in measured and predicted isentropic conditions in the core region of the test section.²⁸ The characterization studies further show that the isentropic core region extends across 70% of the diameter of the test section and that the bulk of the pressure rise (~80%) and temperature rise (~50%) occurs during the last 10 ms of the compression process, where the total stroke lasts approximately 145 ms. An additional important outcome of trapping the cold boundary layers outside the test section is that heat losses from the gases in the core region are minimized, which maximizes the amount of time the test gases are at uniform state conditions. Consequently, conditions can be maintained for long test times on the order of 50 ms, with pressure >75% of EOC pressure and temperature >80% of EOC temperature, depending on the test gas mixtures.

For this study, mixtures were prepared external to the UM RCF to ensure good reactant mixing and uniform composition for each experiment. Stoichiometric *n*-butanol/O₂ (*n*-butanol—Sigma-Aldrich, purum, >99% GC grade; O₂—Cryogenic Gases, Purity Plus 4.3, 99.993%, <40 ppm Ar, <3 ppm moisture, <10 ppm N₂, <0.5 ppm hydrocarbons) mixtures, with an inert/O₂ ratio of 5.64, were prepared manometrically using a mixing manifold and mixing tank that are connected to the UM RCF. Mixture compositions were determined using partial pressures measured with a capacitance diaphragm gauge (Varian Cerami-Cel VCMT12TFA, with an accuracy of ± 0.01 Torr). All mixtures were allowed to mix diffusively for over 12 h. The partial pressure of *n*-butanol used in the mixtures was maintained at less than half the saturation vapor pressure of *n*-butanol at room temperature (8.81×10^{-3} atm or 6.69 Torr at 25 °C) to avoid concerns of fuel condensation. The concentration of inert gases in the mixture—Ar (Cryogenic Gases, Purity Plus 5.0, 99.999%, <2 ppm O₂, <2 ppm moisture, <0.5 ppm hydrocarbons) and N₂ (Cryogenic Gases, Purity Plus 5.0, 99.999%, <2 ppm O₂, <3 ppm moisture, <0.5 ppm hydrocarbons)—was varied to control the ratio of specific heats of the reactant mixture and thereby the EOC state conditions. Total mixture pressures in the mixing tank were 0.11–0.13 atm, and each mixture was typically used for two ignition experiments with initial fill pressures (P_0) in the RCF of $P_0 = 3.2 \times 10^{-2}$ – 3.7×10^{-2} atm.

The test section is instrumented with several diagnostics to interrogate the test gas mixture during ignition studies. The pressure in the test section is monitored using a piezoelectric transducer (Kistler 6041AX4) and charge amplifier (Kistler 5010B) with a combined accuracy of 0.01 atm and 0.015 ms. All electronic signals are acquired using a data acquisition system (National Instruments (NI) cDAQ 9172 chassis coupled with NI 9215 cards) recording at 100 kHz. High-speed imaging of the combustion phenomena in the test section can be obtained either by viewing along the axis of the test section (end-view) using a transparent end wall or orthogonal to the axis of the test section (side-view) using a transparent cylindrical section. For this study, a high-speed CMOS camera (Vision Research, Phantom v7.1, SR-CMOS 48-bit color array, maximum resolution of 800 × 600 pixels, capable of 160 kHz at reduced spatial resolution, 22 μm pixels with 0.34 μm spacing) was used to record end-view images during ignition. Side-view imaging was not used. The chemiluminescence from the test volume was captured with a fast 50 mm lens (f/0.95, Navitar) and c-mount extension tube. For these experiments, a setting of 26 000 frames per second (fps) with an image exposure time of 38 μs and a spatial resolution of 256 × 256 pixels was used. The imaging data provide qualitative and quantitative indications of the ignition homogeneity. The camera

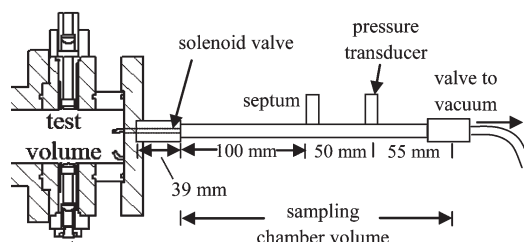


Figure 3. Schematic of the rapid gas-sampling system used in the current work.

array records color signals using red ($\sim 95\%$ transmission above 615 nm), blue ($\sim 86\%$ peak transmission at 460 nm), and green ($\sim 82\%$ peak transmission at 530 nm) spectral filters. No additional spectral filtering was used.

2.2. High-Speed Gas Sampling and Gas Chromatography.

For the high-speed gas sampling experiments, the transparent end wall was replaced with an end wall equipped with a gas sampling system. For the sampling experiments, a small portion of the test gas mixture is removed from the test section through the end wall (as shown in Figure 3) at targeted time intervals during the ignition delay period. The gas samples are then analyzed to identify and quantify the species present. By conducting a series of RCF ignition experiments at the same targeted EOC conditions, the overall species time histories for the intermediates are compiled.

Previous studies to investigate the intermediates formed during *iso*-octane and methyl butanoate ignition delay times have been conducted using rapid gas sampling from UM RCF experiments.^{23,26} For this work, the same sampling approach was used, but a new four-valve gas-sampling system was created to improve the time response (via custom-modified valves) and decrease the level of dilution of the sample gases (via decreased dead volume in the sampling system and with the potential to acquire larger gas samples in the same sampling time). These modifications reduce the uncertainty in the species measurements. The new gas-sampling system also allows gas sampling at higher EOC pressures (up to approximately 10 atm).

The major components of the sampling system are the sample chambers (4.5 ± 0.5 mL), piezoresistive pressure transducers (Kistler 4045A2) and amplifiers (Kistler 4618A0), septa (VICI Valco, low-bleed), four fast-acting sampling valves (modified Festo MHE3 valves with a stock response time of 3 ms, 3 mm orifice), and four vacuum isolation valves (Swagelok). A schematic of the sampling system is shown in Figure 3. Up to four samples can be obtained per experiment through independent control of each sampling valve, triggered using two pulse generators (Stanford Research Systems model DG535 Digital Delay/Pulse Generators). The four samples are acquired through probes located on a square spacing (26×26 mm) on the end wall, 19 mm (radially) from the center of the test section (recall the test section i.d. is 50.8 mm). For the high-speed sampling data presented in this paper, two gas samples were acquired in each experiment by triggering two of the fast-acting valves located at the northeast and southwest positions, 180° from each other. Each sampling tube connected to the fast-acting valve extends approximately 10 mm from the end wall into the test section, well beyond the cold thermal boundary layer of the test section end wall. Experiments were performed to ensure the sampling end wall has no effect on the ignition kinetics of *n*-butanol. Specifically, τ_{ign} were measured with the sampling end wall in place without triggering the sampling valves. The measured values for τ_{ign} were identical to the

measurements made with the imaging end wall. In addition, by acquiring small samples (as opposed to quenching the entire test volume), the ignition characteristics of each experiment remain unaffected. As will be shown below, τ_{ign} values determined from the gas-sampling experiments were in excellent agreement with experiments where gas sampling was not used.

A primary source of uncertainty in the gas-sampling measurements is the dilution of the gas samples with unreacted gases present in dead volume of the gas-sampling system. Specifically, the cold unreacted gases (essentially unreacted test gas mixture) initially present in the sampling probes are also acquired in the sampling chamber when the sampling valves are opened. The unreacted test gases dilute the concentration of the gases taken from the hot core region of the test section, and the reactant mixture can cause interference in the chromatograms. To quantify these effects, pyrolysis experiments were performed using EOC conditions that would consume all of the fuel in the reactive core before the gas samples were acquired. Any measured fuel would then be from the dead volume, and quantifying the fuel yields an accurate estimate of the dilution of the gases sampled from the core of the test section. For this work, pyrolysis experiments using *n*-butanol were used and compared to results obtained from previous characterization work for pyrolysis of C₂ hydrocarbons on the UM RCF.²⁹ Model predictions show that less than 0.3% of *n*-butanol would remain in the core region of the test section at 11.2 ms after the end of compression for EOC conditions of $T = 1400$ K and $P = 3.25$ atm. The *n*-butanol and C₂ pyrolysis experiments show that the dilution ranges between 5 and 16%, depending on the temperature conditions in the test section. The data for this study were analyzed using 16% dilution by the unreacted test gas mixture.

Another source of uncertainty in the gas-sampling measurements is due to nonuniformities potentially present in the test section or variability in the different gas-sampling systems. The high-speed imaging provides data on the quality of the spatial uniformity of the ignition characteristics. However, end-view imaging cannot be conducted simultaneously with gas-sampling through the end wall. Consequently, experiments were performed in which the two sampling valves were triggered at the same time such that the two gas samples had the same time history but were obtained from two different locations in the test section. The samples yielded nearly identical concentrations (less than 4% difference) for the species measured.

The temporal resolution of the gas-sampling measurements is limited by the fast-acting valves. Triggering circuits are used to open and close the gas-sampling valves at specified times during the ignition delay time. During the initial part of the triggering signal, the valves stay closed due to inertial effects. At the end of the triggering signal, the sampling valves are fully open and do not shut until the spring inside the valve body is extended. This results in a valve opening time of approximately 1.5 ms centered on the end of the valve-sampling signal. During the sampling event, the gases are quickly quenched (<0.3 ms) as they expand into the vacuum of the sample chamber ($P_{\text{test section}}/P_{\text{sample chamber}} \sim 11$, $V_{\text{test section}}/V_{\text{sample chamber}} \sim 39$). The gas-sampling results therefore represent the average value of the species during the sampling time. Once the samples are acquired, the gases are drawn into a syringe (Hamilton Gastight #1010, 10 mL) through the syringe port on the sampling chamber for delivery to the gas chromatograph.

The gas chromatograph (GC) was calibrated for quantitative measurements of the species of interest, namely, *n*-butanol

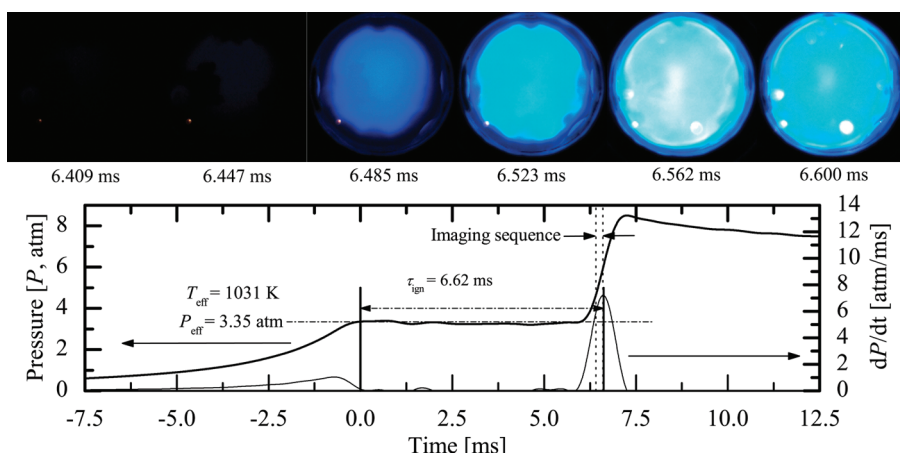


Figure 4. Results for a typical *n*-butanol ignition experiment with $P_{\text{eff}} = 3.35 \text{ atm}$, $T_{\text{eff}} = 1031 \text{ K}$, $\phi = 1$, inert/O₂ = 5.64, and $\tau_{\text{ign}} = 6.6 \text{ ms}$. The lower panel shows the pressure (P) and the rate of pressure rise (dP/dt) in the test section. End of compression is set as time $t = 0 \text{ ms}$. The upper panel shows the corresponding still images (end view), acquired at 26 000 fps, of the chemiluminescence during ignition (no color adjustment).

(*n*-C₄H₉OH), methane (CH₄), carbon monoxide (CO), ethene (C₂H₄), propene (C₃H₆), acetaldehyde (CH₃CHO), 1-butene (1-C₄H₈), and *n*-butyraldehyde (*n*-C₃H₇CHO). The GC system (PerkinElmer Autosystem) was equipped with a flame ionization detector (FID, air/hydrogen flame) and a thermal conductivity detector (TCD). A Restek RTX-1 capillary column was used to measure both pure hydrocarbons as well as oxygenated hydrocarbons (using the FID detector), and a Restek ShinCarbon ST packed column was used to measure CO (using the TCD detector). The columns were maintained in the GC oven at 50 °C with ultra high purity helium (Cryogenic Gases, Purity Plus, 99.999%) as the carrier gas. The helium, air, and hydrogen were further purified before use in the GC using adsorbents to remove water, hydrocarbons, and oxygen. The FID detector was maintained at 300 °C, with an attenuation of 1 and a range of 1. The TCD detector was maintained at 50 °C with an attenuation of 1 and a current of +160 mA. Split injection was used to introduce the analytes into the columns, with less than 0.5 mL of sample introduced into the septum and the sample loop being 5 μL. High-purity reference chemicals were characterized for the GC temperature programs used in the study, and the chromatograms were used to establish the calibrations for absolute concentration. Calibration gases were used for CH₄ (Cryogenic Gases, chemically pure, 99%), CO (Matheson, ultrahigh purity, 99.9%), C₂H₄ (Matheson, chemically pure, 99.5%), C₃H₆ (Cryogenic Gases, polymer grade, 99.5%), and 1-C₄H₈ (Cryogenic Gases, 99%). CH₃CHO was calibrated using the vapor of liquid CH₃CHO (Fluka, puriss. p.a., anhydrous, >99.5% GC grade, ≤0.5% free acid CH₃COOH), and *n*-C₃H₇CHO was calibrated using the vapor of liquid *n*-C₃H₇CHO (Fluka, puriss., ≥99% GC grade, ≤1% butyric acid, <0.1% BHT as a stabilizer, <1% H₂O as a stabilizer). Calibration mixtures were made in a mixing tank with the upper limit of concentrations calibrated for being greater than the maximum concentrations predicted by the Black et al.¹ mechanism for the ignition delay of a mixture with $\chi(n\text{-but}) = 0.025$, $\chi(\text{O}_2) = 0.147$, $\chi(\text{N}_2) = 0.541$, and $\chi(\text{Ar}) = 0.288$ at $P = 3.25 \text{ atm}$ and $T = 975 \text{ K}$. Calibration curves were linear in all cases. Measurements of *n*-butanol were of interest for this work, and *n*-butanol was well isolated in the chromatograms. However, calibration experiments showed the *n*-butanol (Sigma-Aldrich, purum, >99% GC grade, <0.1% H₂O) features were a nonlinear function of the GC-FID detector, and the *n*-butanol saturated the FID detector for mole fractions of 0.5% and

higher. Consequently, potential *n*-butanol measurements were limited to levels below 0.5% for this study. Signals from the GC detectors were recorded using a high-resolution data acquisition system (NI PXI 4472) with a sampling rate of 8 Hz. A temperature-controlled 10-port valve was used to direct the samples into the GC.

3. EXPERIMENTAL RESULTS AND DISCUSSION

3.1. Ignition Experiments. Figure 4 presents typical results from a UM RCF *n*-butanol ignition experiment. The time histories of the pressure (P) and rate of pressure rise (dP/dt) in the test section are shown in the lower panel. High-frequency (>2.5 kHz) disturbances generated by the impact of the sabot near the EOC are filtered from the pressure time histories using a fast Fourier transform. The pressure data show the compression process is smooth with no indications of disturbances or abrupt fluctuations. The pressure reaches the first maximum due to compression by the sabot, and the EOC is set to time $t = 0$, after which the volume in the test section is constant. After a period of time where the pressure remains nearly constant, the pressure increases rapidly to a second maximum due to ignition of the fuel/oxidizer/diluent mixture.

The upper panel of Figure 4 shows stills from the imaging sequence of the chemiluminescence emitted during ignition. The chemiluminescence is only observed during the high rates of pressure rise that occur during ignition. The emission is attributed to CH and C₂ radicals due to the strong spectroscopic features of these species in the blue (CH: 431.2 nm; C₂: 473.7 nm, 516.5 nm, 563.5 nm) and because CH and C₂ are generated through the decomposition of intermediate hydrocarbons present in the fuel/oxidizer/diluent mixture. Note the intense blue emission occurs throughout the test section with uniform intensity, indicating good homogeneity of the reactant mixture and of thermal conditions in the test section.

For each experiment, the effective test conditions are determined using the same methods as in previous UM RCF experiments²¹ and are based on the pressure time history from each experiment. The effective pressure (P_{eff}) is defined by Equation 1 as the time-integrated average pressure from the maximum pressure (P_{max}) at EOC to the maximum of rate of

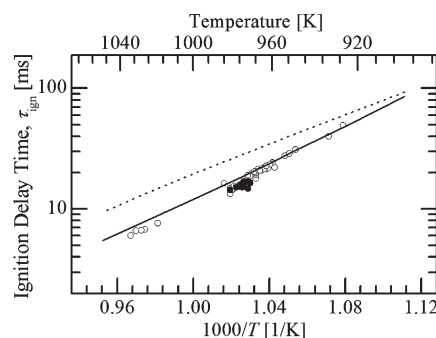


Figure 5. Comparison of experimental results for *n*-butanol ignition delay time measured in the current work with model predictions ($P = 3.25$ atm) based on the reaction mechanisms developed by Black et al.¹ (solid line) and Veloo et al.⁵ (dotted line). All results presented are for $\phi = 1$, inert/O₂ = 5.64. ○, Current work, $P = 2.9$ –3.4 atm; ●, Current work, gas-sampling experiments, $P = 3.22$ –3.34 atm.

pressure rise (dP/dt_{\max}).

$$P_{\text{eff}} = \frac{1}{t_{\text{dp}/dt_{\max}} - t_{P_{\max}}} \int_{t_{P_{\max}}}^{t_{\text{dp}/dt_{\max}}} P \cdot dt \quad (1)$$

The effective temperature for each experiment is determined using P_{eff} and numerical integration of the isentropic relation (eq 2)

$$\int_{T_0}^{T_{\text{eff}}} \frac{\gamma}{\gamma - 1} d \ln T = \ln \left(\frac{P_{\text{eff}}}{P_0} \right) \quad (2)$$

where P_0 is the initial charge pressure, T_0 is the initial temperature, and γ is the temperature-dependent ratio of the specific heats of the unreacted test gas mixture (determined using the NASA thermodynamic database³⁰). The ignition delay time, τ_{ign} , for each experiment is defined as the time between EOC ($t = 0$ ms, defined by the first maximum in P) and dP/dt_{\max} .

n-Butanol ignition experiments were performed in a narrow pressure range (2.9–3.4 atm) between temperatures of 920 and 1040 K. The equivalence ratio (ϕ , defined as the ratio of (fuel/O₂)_{actual}/(fuel/O₂)_{stoichiometric}) was $\phi = 1$, and the dilution (with nitrogen and argon being the sole diluents for all experiments) was inert/O₂ = 5.64 for all experiments. The *n*-butanol concentration for the experiments was 2.4–2.5%. Table S1 found in the Supporting Information accompanying this paper is a summary of the experimental conditions and results for τ_{ign} , and Figure 5 shows τ_{ign} as a function of temperature for *n*-butanol on an Arrhenius diagram. The open symbols are the results of experiments where the transparent end wall was used. The filled symbols are the results of gas-sampling experiments. The ignition data for both sets of experiments follow typical Arrhenius behavior (with no negative temperature coefficient region expected or observed) and are in excellent quantitative agreement with each other. Hence, as noted earlier, the effects of sampling on the ignition behavior of the test gas mixtures are negligible.

The uncertainty in the measured τ_{ign} is primarily due to the uncertainty in the effective temperature, which is calculated using the measured pressure and Equation 2. The accuracy of the pressure transducer is $\pm 0.5\%$. This translates to approximately $\pm 0.2\%$ variation in T_{eff} . The random error in the measured τ_{ign} is estimated using the standard deviation of the data for the temperature range 972–978 K which is 1.3 ms or $\pm 8\%$. A conservative estimate for the overall uncertainty for τ_{ign} for the

entire temperature range is $\pm 15\%$, which is the maximum scatter in the data at any of the temperatures investigated.

The experimental results for τ_{ign} are also compared in Figure 5 to model predictions from two recently published *n*-butanol reaction mechanisms. Veloo et al.⁵ developed a mechanism specifically for atmospheric pressure flames, with 266 species and 1639 reactions. Black et al.¹ developed a mechanism based on C₄ chemistry¹⁹ with an *n*-butanol submechanism, for a wide temperature (740–1660 K) and pressure range (1–34 atm). In total, their mechanism consists of 234 species and 1399 reactions. The two reaction mechanisms were used to predict τ_{ign} using the CHEMKIN suite of programs and assuming a zero dimensional, spatially homogeneous, adiabatic constant volume system. For the simulations, τ_{ign} was defined as the time from the start of the simulation to the maximum rate of pressure rise. The input conditions for the model simulations were mixture compositions and the effective temperatures and pressures are listed in Table S1 (Supporting Information). As seen in Figure 5, *n*-butanol ignition delay is quite linear on an Arrhenius scale with no negative temperature coefficient region expected or observed. In addition, there is excellent agreement between the results based on the reaction mechanism developed by Black et al.¹ and the experimental data. Specifically, the reaction mechanism by Black et al.¹ predicts τ_{ign} to within 20% for temperatures higher than approximately 960 K and to within 10% for temperatures below 960 K. The model results using the reaction mechanism by Veloo et al.⁵ are also in good agreement with the experimental data, well within a factor of 2 for most temperatures.

A concern for experiments conducted in rapid compression facilities is the possible reaction of the fuel/oxidizer/diluent mixture during compression, which impacts the assumptions used to define the effective temperature and pressure of the experiments and therefore the input conditions to the CHEMKIN simulations. Experimentally, such concerns can be investigated by performing non-igniting experiments, where the O₂ is replaced by N₂ in the original fuel/oxidizer/diluent mixture. Such experiments were conducted as part of this study and are presented and discussed with the gas sampling data below. Briefly, the experimental data show negligible deviation in the pressure time history for the non-igniting and the igniting experiments (<1% difference in the effective pressures or pressure time histories to the time of ignition). To further investigate these concerns, the compression process was simulated. Specifically, CHEMKIN simulations were performed representing the compression stroke of the UM RCF for the targeted EOC conditions of $T = 975$ K and $P = 3.25$ atm using the Black et al.¹ reaction mechanism, with initial mole fractions of $\chi(n\text{-but}) = 0.025$, $\chi(\text{O}_2) = 0.147$, $\chi(\text{N}_2) = 0.541$, and $\chi(\text{Ar}) = 0.288$. The results of the simulation for τ_{ign} are within 10% of the results where the compression process was not simulated. In addition, the results show that less than 120 ppm of the *n*-butanol of the test mixture is consumed by EOC, and both the pressure and temperature are within 0.1% of the nonreacting EOC values (see Supporting Information for Figure S1 depicting this simulation). Similarly for target EOC conditions of $T = 1025$ K and $P = 3.25$ atm with initial mole fractions of $\chi(n\text{-but}) = 0.025$, $\chi(\text{O}_2) = 0.147$, $\chi(\text{N}_2) = 0.429$, and $\chi(\text{Ar}) = 0.399$, τ_{ign} is faster by less than 10% when the compression stroke is included in the simulation, with less than 1300 ppm of the *n*-butanol in the test mixture consumed by EOC. As with the lower temperature simulation, both the pressure and temperature are within 0.1% of the nonreacting EOC values (see Supporting Information for

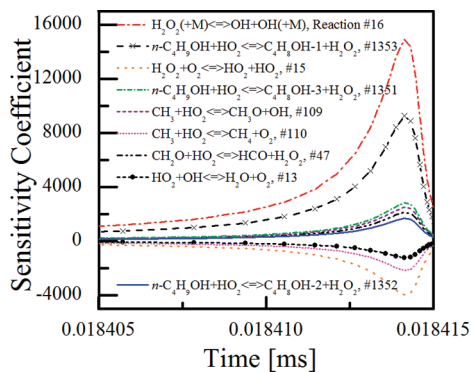


Figure 6. Results for OH sensitivity analysis using the mechanism of Black et al.¹ for the target gas-sampling conditions of $\phi = 1.0$, $T = 975$ K, $P = 3.25$ atm, and inert/O₂ = 5.64.

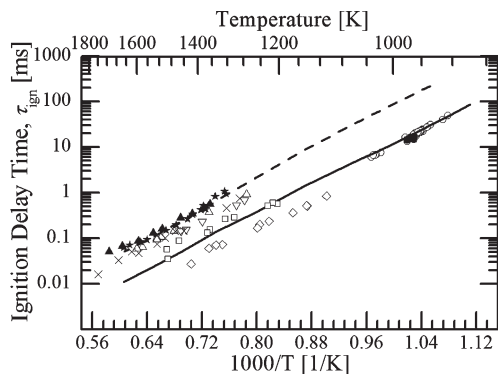


Figure 7. Comparison of the *n*-butanol ignition delay times measured in the current work with the experimental results for shock tube studies of *n*-butanol ignition by Moss et al.⁸ and Black et al.,¹ where $\phi = 1$ for all data. ○, Current work, $P = 2.9$ – 3.4 atm, inert/O₂ = 5.64; ■, current work, gas-sampling experiments, $P = 3.22$ – 3.34 atm, inert/O₂ = 5.64; △, Moss et al.,⁸ $P = 1$ atm, inert/O₂ = 15.5; ▲, Moss et al.,⁸ $P = 1.3$ atm, inert/O₂ = 32; ▽, Moss et al.,⁸ $P = 4$ atm, inert/O₂ = 65.7; ★, Black et al.,¹ $P = 1$ atm, inert/O₂ = 21; ×, Black et al.,¹ $P = 2.5$ – 3.1 atm, inert/O₂ = 26.6; □, Noorani et al.,¹¹ $P = 1.8$ – 2.5 atm, inert/O₂ = 10; ◇, Noorani et al.,¹¹ $P = 1.8$ – 2.5 atm, inert/O₂ = 10. Model predictions based on the Black et al.¹ mechanism are presented for conditions of $P = 1$ atm, inert/O₂ = 21 (dashed line), and $P = 3.25$ atm, inert/O₂ = 5.64 (solid line).

Figure S2 depicting this simulation). The results confirm that reaction during compression is of little concern for the ignition delay time experiments or the gas-sampling experiments.

Sensitivity analysis was used to identify the reactions having a significant effect on *n*-butanol ignition delay time. The analysis was performed using the initial conditions of $T = 975$ K, $P = 3.25$ atm, $\chi(n\text{-but}) = 0.025$, $\chi(\text{O}_2) = 0.147$, $\chi(\text{N}_2) = 0.541$, and $\chi(\text{Ar}) = 0.288$ ($\phi = 1.0$, inert/O₂ dilution = 5.64) using the Black et al.¹ mechanism. The OH radical concentration was used as a surrogate for ignition delay time, and the results of the OH sensitivity analysis are presented in Figure 6. The most important reaction is the chain-initiating decomposition of H₂O₂ into two OH radicals. The *n*-butanol + HO₂ reaction also plays a large role at these conditions as a source of H₂O₂. These results differ from those of Black et al.,¹ who also performed sensitivity analysis for *n*-butanol ignition and found the chain branching H + O₂ reaction to be the most important. The results highlight the change in the reaction kinetics from the lower temperatures

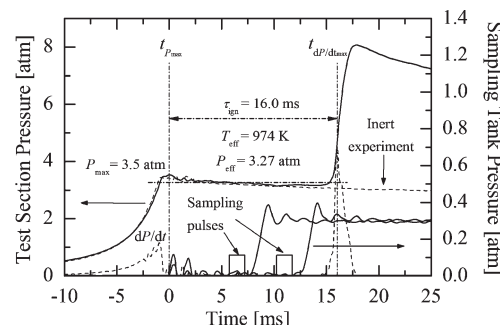


Figure 8. Results for a typical *n*-butanol ignition experiment with gas sampling during the ignition delay period. The pressure and pressure derivative time histories in the test section and in the two sampling chambers are presented. The triggering signals for the rapid gas sampling valves are also provided. The pressure time history for a non-igniting (i.e., inert) experiment is included for comparison.

considered here (975 K), where competition between H₂O₂ and HO₂ chemistry dominates the ignition chemistry, to the higher temperatures considered by Black et al.¹ (1450 K), where H, OH, and O are the radical chain carriers.

Figure 7 presents the experimental data from the current work and the previous shock tube studies by Black et al.,¹ Moss et al.,⁸ and Noorani et al.¹¹ The shock tube data were obtained at higher temperatures and dilution levels than the current study and span pressures from 1 to 4 atm. Zero dimensional, spatially homogeneous, adiabatic, constant volume model predictions based on the reaction mechanism by Black et al.¹ are also shown in the figure. Model predictions for the shock tube data (with $\chi(n\text{-but}) = 0.008$, $\chi(\text{O}_2) = 0.045$, $\chi(\text{Ar}) = 0.948$, $P = 1$ atm) span the dilution (composition and levels) and pressures of the experimental shock tube data for the extended temperature range $T = 950$ – 1650 K. Model predictions for the UM RCF data (with $\chi(n\text{-but}) = 0.025$, $\chi(\text{O}_2) = 0.147$, $\chi(\text{N}_2) = 0.541$, and $\chi(\text{Ar}) = 0.288$, $P = 3.25$ atm) are presented for the extended temperature range $T = 900$ – 1650 K. The model predictions are in excellent agreement with both data sets, and they reproduce the shift to faster ignition that occurs with higher concentrations of fuel in the reacting mixtures and with slightly higher pressures.

3.2. High-Speed Gas Sampling Experiments. The ignition delay time study provided the basis to identify thermodynamic conditions where high-speed gas sampling could be applied with good accuracy and repeatability. On the basis of these results, EOC temperatures of $T_{\text{eff}} = 975$ K were targeted for the gas-sampling experiments. Specifically, UM RCF experiments with $T_{\text{eff}} = 975$ K yielded ignition delay times between 14 and 17 ms, allowing a sampling time resolution of approximately 10:1. Results from a typical sampling experiment are presented in Figure 8, where $P_{\text{eff}} = 3.27$ atm, $T_{\text{eff}} = 974$ K, and $\tau_{\text{ign}} = 16.0$ ms. Figure 8 includes the time histories of the pressure and pressure derivative in the test section, the two triggering signals of the gas-sampling system, and the pressures in the two sampling chambers. As seen in the figure, the pressure in the test section is unaffected by the sampling process, and the features are similar to the data of Figure 4, which shows ignition without gas sampling. The time histories of the two gas samples show the rapid increase in pressure that occurs after the triggering signals and confirm the sampling times as <2 ms. Figure 8 also includes for comparison the pressure time history for a non-igniting experiment (labeled "Inert experiment") with the same thermal characteristics as an

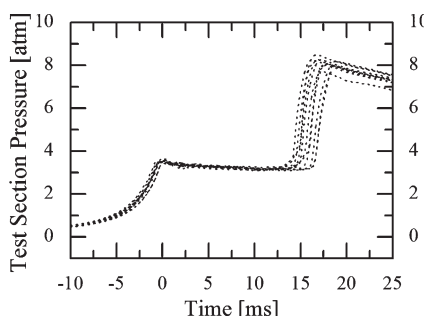


Figure 9. Comparison of the pressure time histories for the high-speed gas-sampling experiments of *n*-butanol ignition. Note the nearly identical compression processes for all experiments.

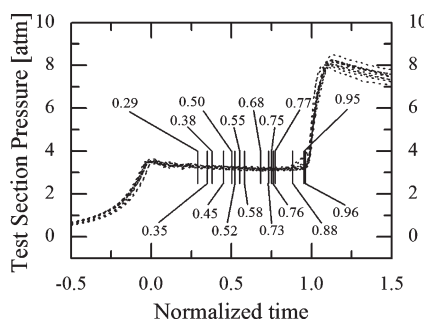


Figure 10. Comparison of the pressure time histories of the sampling experiments on a time scale normalized to τ_{ign} for each experiment. The normalized time for each gas-sample measurement is labeled in the figure.

igniting *n*-butanol/oxidizer/diluent mixture (where the O₂ in the mixture has been replaced with N₂). The non-igniting pressure time history is virtually indistinguishable from the igniting pressure time history (where P_{eff} and T_{eff} differ by less than 1% and 0.5%, respectively). The comparison demonstrates that neither the ignition chemistry nor the gas sampling affects the heat transfer physics of the experiments.

A total of 11 gas-sampling experiments were performed. A summary of the experimental conditions, the measured τ_{ign} , and the sample times are provided in Table S2, found in the Supporting Information. A summary of the pressure time histories of the gas-sampling experiments is presented in Figure 9. All of the sampling experiments show nearly identical, smooth compression processes. The slight decrease in pressure after EOC (due to heat losses to the test manifold walls, prior to the sampling events) is also extremely consistent between experiments. The averages and standard deviations for the EOC conditions and measured τ_{ign} are provided in Table S2 (Supporting Information). The standard deviations of the EOC pressures, P_{eff} , and τ_{ign} for the sample experiments are 0.06 atm, 0.04 atm, and 0.84 ms, respectively.

While the data of Figure 9 and Table S2 (Supporting Information) demonstrate the excellent level of repeatability of the sampling experiments, there are slight differences in the EOC conditions and ignition delay times. To compensate for these slight differences in the experimental pressure time histories, the sampling data are reported using a time domain that is normalized by the actual τ_{ign} for each experiment. EOC is defined as $t/\tau_{\text{ign}} = 0$, and $t/\tau_{\text{ign}} = 1$ is the time of ignition. Figure 10 presents the pressure time histories of Figure 9 after normalizing by the

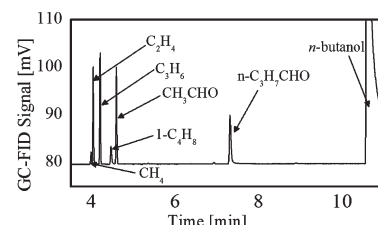


Figure 11. Typical GC-FID chromatogram results of a gas sample acquired at $t = 7.2$ ms, $t/\tau_{\text{ign}} = 0.45$, for experimental conditions of $P_{\text{eff}} = 3.27$ atm, $T_{\text{eff}} = 974$ K, and $\tau_{\text{ign}} = 16.0$ ms.

τ_{ign} for each experiment. The normalized times when each gas sample was taken during the ignition delay period are labeled in the figure. Note that due to the low levels of intermediate species at early times the sampling data were preferentially acquired closer to the time of ignition.

Figure 11 shows a typical GC-FID chromatogram from an *n*-butanol ignition experiment for conditions of $P_{\text{eff}} = 3.27$ atm, $T_{\text{eff}} = 974$ K, $\tau_{\text{ign}} = 16.0$ ms, and a sampling time of 7.2 ms. Peaks from CH₄, C₂H₄, C₃H₆, CH₃CHO, 1-C₄H₈, *n*-C₃H₇CHO, and *n*-butanol are identified in the figure. CO measurements were made using chromatograms from the GC-TCD detector and are not shown here. All major features on the chromatograms were identified. Using the calibration data for each species and the measured dilution levels of the gas samples, the chromatograms were converted into discrete measurements for each sampling time. Figure 12 presents the results for the eight intermediate species as a function of the normalized ignition delay time for the nominal experimental conditions of $P_{\text{eff,average}} = 3.29$ atm and $T_{\text{eff,average}} = 975$ K. In Figure 12, the error bars are the uncertainty in the experimental data. As described above, the uncertainty in the sampling times is ± 0.75 ms, or approximately ± 0.05 when normalized by the average ignition delay time. The uncertainty in the measured mole fractions was $\pm 16\%$ as determined by the uncertainty in the species calibration and dilution percentage, as discussed earlier. The calibration and dilution were considered independent sources of uncertainty, and the overall uncertainty for each species was determined using the square root of the sum of the squares for each source of uncertainty. Note that only two measurements were above the detectable limit for CO, and none of the *n*-butanol measurements were both below the limit that saturated the GC detector and above the detectable limit for *n*-butanol, given the uncertainty due to dilution.

Results for the model predictions using the reaction mechanism by Black et al.¹ for the initial condition of $P = 3.25$ atm, $T = 975$ K, inert/O₂ = 5.64, and *n*-butanol = 2.45% are presented as the solid lines in Figure 12. The predicted ignition delay time is $\tau_{\text{ign}} = 18.6$ ms, which is within 18% of the average of the experimental data ($\tau_{\text{ign,average}} = 15.7$ ms). The model predictions show good qualitative agreement with the experimental data for all species. The quantitative agreement is very good (within a factor of 2 for the duration of the ignition delay period) for CH₄. However, the model significantly overpredicts C₂H₄ (by a factor of 4–8 over the entire ignition delay period) and C₃H₆ (by a factor of 2–3 over the ignition delay period). 1-C₄H₈ shows good quantitative agreement, with differences less than a factor of 2 over most of the ignition delay period. CO was measured at detectable levels in the GC-TCD chromatograms only closer to ignition, as predicted by the model. Note that the model

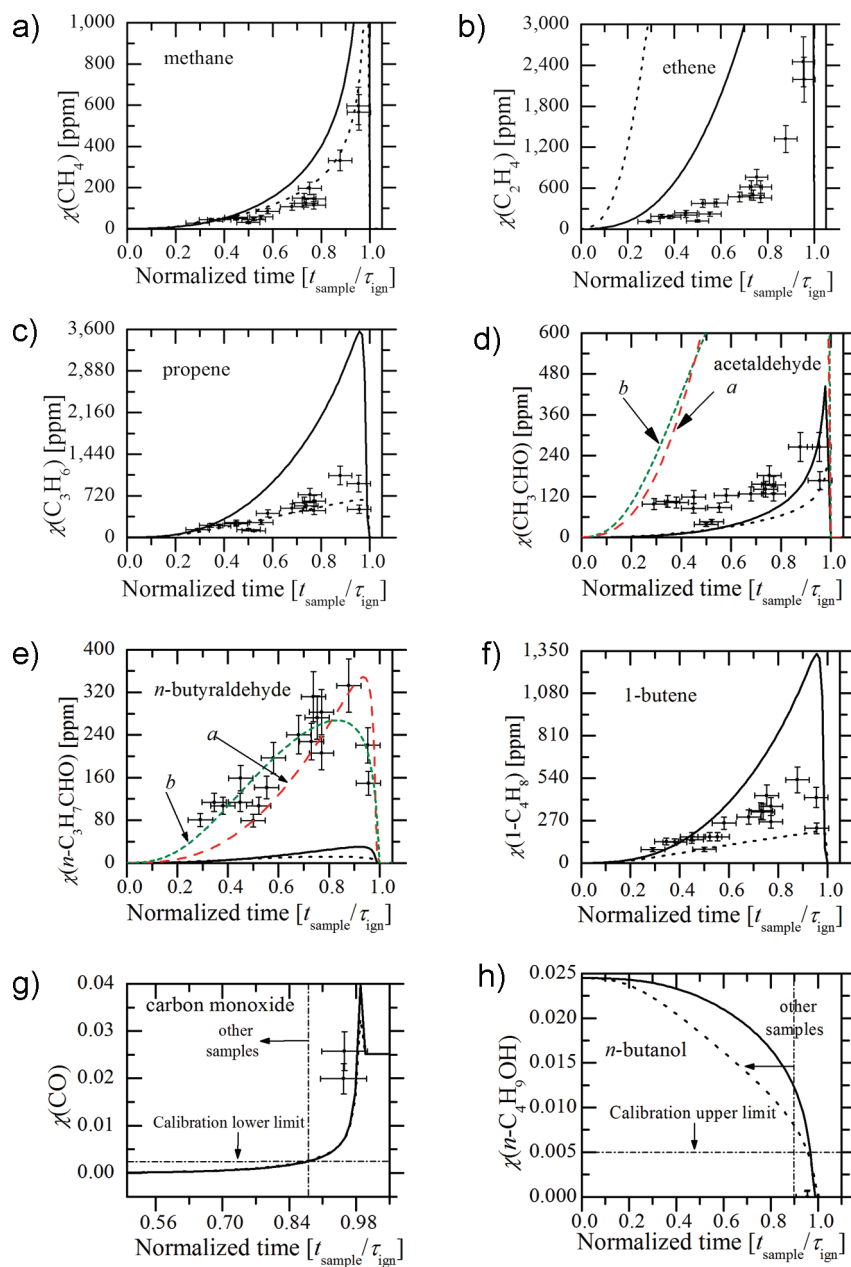


Figure 12. Comparison between measured intermediate species and model predictions using the reaction mechanism of Black et al.¹ and the initial conditions of $P = 3.25$ atm, $T = 975$ K, inert/O₂ = 5.64, and *n*-butanol = 2.45% ($\tau_{\text{ign,predicted}} = 18.6$ ms). The unmodified mechanism predictions are shown with solid lines, and the modified mechanism predictions are shown with dotted black lines. The average experimental conditions are $P_{\text{eff}} = 3.29$ atm, $T_{\text{eff}} = 975$ K, inert/O₂ = 5.63, and *n*-butanol = 2.44% ($\tau_{\text{ign,average}} = 15.7$ ms). The error bars represent the experimental uncertainties. The time domain has been normalized from $t/\tau_{\text{ign}} = 0$ (end of compression) to the time of ignition, $t/\tau_{\text{ign}} = 1$.

predictions show a narrow peak for CO, where it is formed rapidly and consumed rapidly very close to ignition. The model predictions for CO are within the experimental uncertainties when the temporal resolution of the experimental data is considered. Similarly, the model predictions for *n*-butanol are consistent with expectations based on the limiting factors for the measurements. Specifically, for times less than $t/\tau_{\text{ign}} \sim 0.95$ the experimental data for *n*-butanol are limited by the 0.5% threshold for the GC-FID detector. Quantitative measurements of CO₂ can be made using the GC configuration used in the current work. However, no CO₂ peaks were observed at any sampling conditions. The absence of CO₂ is consistent with the

predictions which indicate CO₂ levels will not exceed the minimum detectable limit of 0.25% until times after $t/\tau_{\text{ign}} > 0.98$. The aldehydes calibrated for and measured, CH₃CHO and *n*-C₃H₇CHO, warrant a more detailed discussion, particularly with reference to enol-keto isomerization (tautomerization) as described by Black et al.¹ and Harper et al.³¹ This discussion is presented later.

The experimental data capture a reasonable fraction of the carbon in the system. By comparison with the model predictions for the concentrations of carbon-containing species, the GC measurements account for 54–75% of the carbon *not* present in *n*-butanol at early sampling times ($t/\tau_{\text{ign}} < 0.4$) and 15–48% of

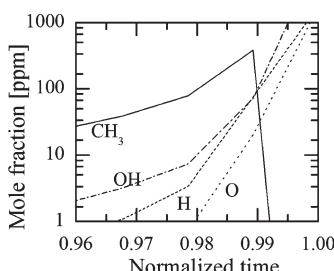


Figure 13. Species time histories of radicals predicted using the reaction mechanism of Black et al.¹ for initial conditions of $P = 3.25$ atm, $T = 975$ K, inert/ $O_2 = 5.64$, and $n\text{-butanol} = 2.45\%$.

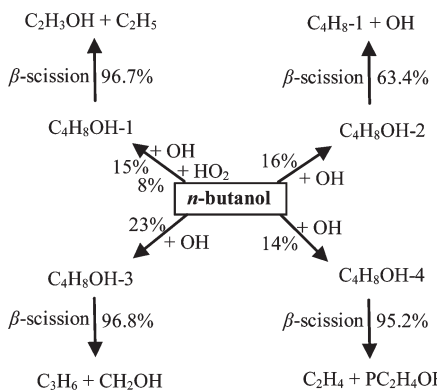


Figure 14. Reaction path diagram of the primary decomposition reactions for *n*-butanol for $t/\tau_{\text{ign}} = 0.75$ and the initial conditions of $P = 3.25$ atm, $T = 975$ K, inert/ $O_2 = 5.64$, and $n\text{-butanol} = 2.45\%$.

this carbon at sampling times closer to ignition ($t/\tau_{\text{ign}} > 0.7$). When CO was measurable ($t/\tau_{\text{ign}} > 0.9$), the GC measurements capture 31–35% of the total carbon present in the system.

During gas sampling, radicals present in the test section are quenched and can be a source of interference with the gas-sampling measurements. For example, radicals such as O, H, OH, and CH₃ can recombine to form water vapor and small hydrocarbons. Radical recombination has potential to affect the GC results by systematically biasing the data by introducing unexpected stable species into the samples or by increasing the concentration of species beyond the levels present before quenching. However, radical recombination is not expected to be a source of error in the current work due to the low levels of radicals present prior to ignition. For example, the predicted time histories for OH, O, H, and CH₃ based on the Black et al.¹ mechanism and the initial conditions $P = 3.25$ atm, $T = 975$ K, inert/ $O_2 = 5.64$, and $n\text{-butanol} = 2.45\%$ are shown in Figure 13. Negligible levels of these radicals (<30 ppm) are predicted for nearly the entire ignition delay time period, i.e., $t/\tau_{\text{ign}} < 0.96$.

Rate of production analysis was used to identify the reaction pathways important for the species measured. The analysis was conducted at 75% of τ_{ign} using the Black et al.¹ mechanism (at the same conditions described above). Figures 14–20 show the primary reaction pathways for the major species (*n*-butanol and CO) and the intermediates. The percentages listed in the figures quantify the specific reaction pathway relative to the overall consumption of the individual species. The results for *n*-butanol (Figure 14) show that H-atom abstraction via OH followed by β-scission to form alkyl radicals and alkenes is the key decomposition pathway for *n*-butanol at these conditions. Figure 15

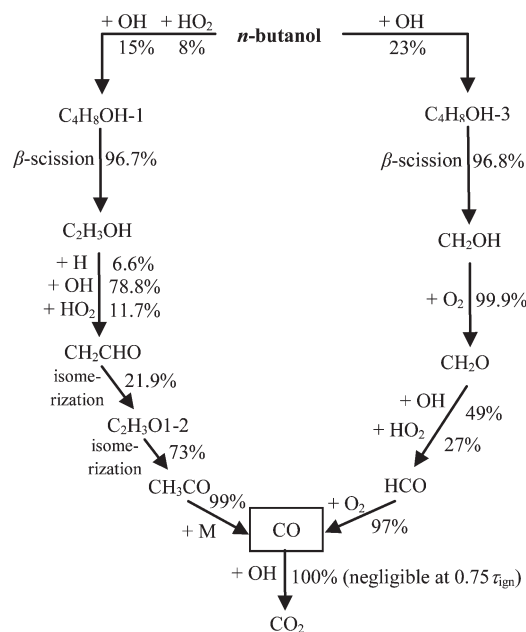
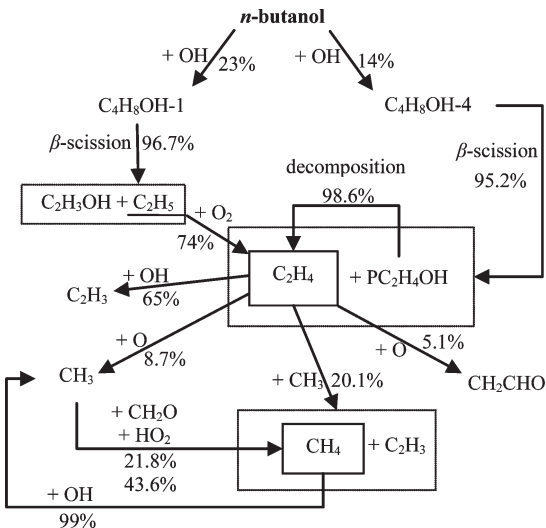


Figure 15. Reaction path diagram of the primary formation pathways for carbon monoxide. Same model conditions as Figure 14.



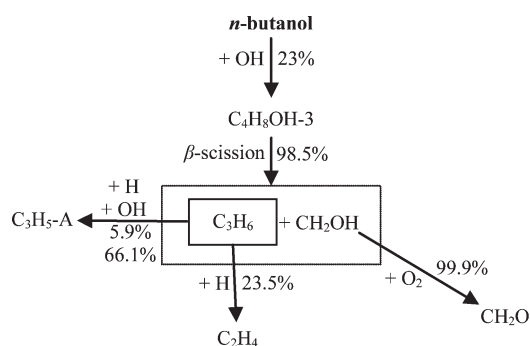


Figure 17. Reaction path diagram of the primary formation and removal pathways for propene. Same model conditions as Figure 14.

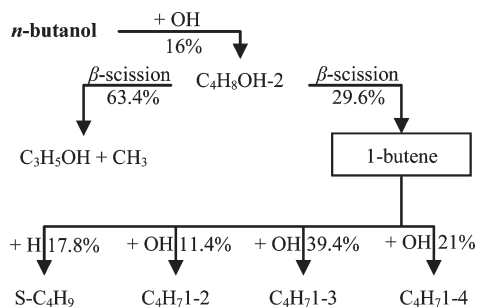


Figure 18. Reaction path diagram of the primary formation and removal pathways for 1-butene. Same model conditions as Figure 14.

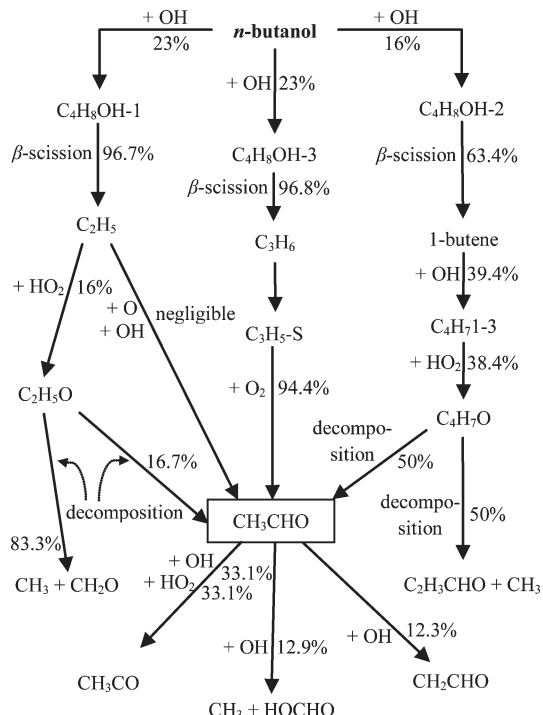


Figure 19. Reaction path diagram of the primary formation and removal pathways for acetaldehyde. Same model conditions as Figure 14.

abstraction from *n*-butanol. *C*₃*H*₆ is predominantly consumed by reactions with H-atoms. Because the model overpredicts *C*₃*H*₆, the rate of production analysis indicates that the branching

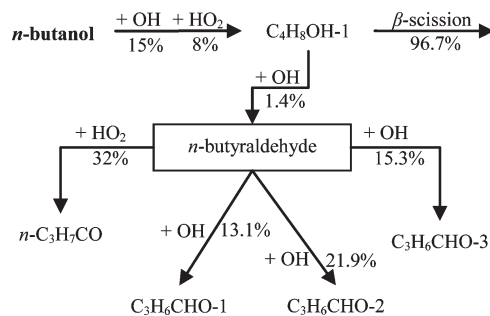


Figure 20. Reaction path diagram of the primary formation and removal pathways for *n*-butyraldehyde. Same model conditions as Figure 14.

fraction for the *C*₄*H*₈OH-3 channel of *n*-butanol decomposition may be slightly too high for the conditions studied here. *1-C*₄*H*₈ (Figure 18) is primarily formed via β-scission of *C*₄*H*₈OH-2, which itself is formed via H-atom abstraction from *n*-butanol. *1-C*₄*H*₈ is consumed by radical abstraction of H-atoms.

Black et al.¹ and Harper et al.³¹ provide detailed descriptions of the tautomerizing of enols to ketones which is relevant to this study. In particular, tautomerization can affect the aldehyde measurements. Black et al.¹ note that the conversion from enol to ketone cannot be easily catalyzed in the gas phase. It is therefore possible that the enol is the preferred low-energy state, as the barrier height for isomerization is approximately 243 kJ/mol.¹ Furthermore, Black et al.¹ point out that these isomers cannot be distinguished by gas chromatographic techniques. Therefore, chromatograms depicting concentrations of aldehydes are likely also influenced by the presence of enols. Figure 19 shows that *CH*₃*CHO* is formed via multiple simultaneous pathways resulting from the breakdown of radicals formed via H-atom abstraction from *n*-butanol. Rate of production analysis for *CH*₃*CHO* shows that at the conditions studied tautomerization of ethenol is not an important pathway for *CH*₃*CHO* production. Furthermore, as seen in Figure 12, *CH*₃*CHO* shows good agreement, qualitatively and quantitatively, over the entire ignition delay period. However, non-negligible amounts (~100 ppm) were observed early in the experiments (*t*/*τ_{ign}* < 0.6), which was not predicted by the model. Plotted in Figure 12 as the red/long dashed line, marked *a*, is also the sum of the isomers of *C*₂*H*₄*O*, namely, *CH*₃*CHO* and ethenol. Ethenol is predicted to be present in high concentrations (>3000 ppm) from the β-scission of *C*₄*H*₈OH-1, for *t*/*τ_{ign}* > 0.9. The Black et al.¹ mechanism also predicts non-negligible amounts of ethenol for *t*/*τ_{ign}* < 0.4. It was observed that even though ethenol may coelute with *CH*₃*CHO*, high concentrations of *C*₂*H*₄*O* isomers were not detected in the gas chromatograms. While the *C*₄*H*₈OH-3 channel for *n*-butanol decomposition is a source of *CH*₃*CHO*, decreasing the branching fraction of the *C*₄*H*₈OH-3 channel, as suggested earlier, should not significantly impact the *CH*₃*CHO* time history as the *C*₄*H*₈OH-3 channel is small relative to the other sources of *CH*₃*CHO*.

n-C₃H₇CHO shows the largest discrepancies (Figure 12) between the model predictions and measurements, where the model under-predicts *n*-C₃H₇CHO by an order of magnitude (by a factor of 10–20 for the duration of the ignition delay period). Figure 20 shows that *n*-C₃H₇CHO is formed solely via H-atom abstraction of one of the decomposition products of *n*-butanol (*C*₄*H*₈OH-1) and is consumed by H-atom abstraction.

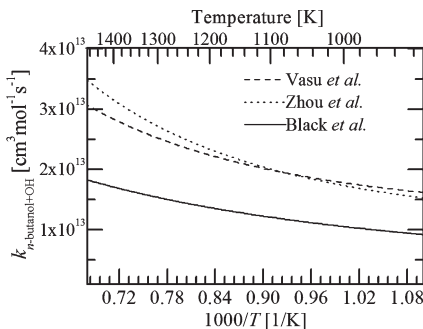


Figure 21. Rate constants for the overall *n*-butanol + OH reaction from Vasu et al.,¹⁵ Zhou et al.,¹⁶ and Black et al.¹

Tautomerization reactions for the conversion of $n\text{-C}_3\text{H}_7\text{CHO}$ to butenols are not included in the Black et al.¹ mechanism. However, just like the case with the $\text{C}_2\text{H}_4\text{O}$ isomers, the $\text{C}_4\text{H}_8\text{O}$ isomers, namely, $n\text{-C}_3\text{H}_7\text{CHO}$, 1-buten-1-ol, 2-buten-1-ol, and 3-buten-1-ol, may coelute and be measured simultaneously with $n\text{-C}_3\text{H}_7\text{CHO}$. When the sum of the concentrations of all the $\text{C}_4\text{H}_8\text{O}$ isomers is plotted in Figure 12 (red/long dashed line, marked *a*), the measured and predicted trends are in very good agreement (generally within the uncertainty limits of the measured data).

The rate coefficient for the reaction of *n*-butanol with OH has been the subject of recent experimental and theoretical studies.^{15,16} Vasu et al.¹⁵ measured the rate constant of the overall reaction of *n*-butanol + OH → products in a shock tube study at pressures of 2.25 atm for temperatures between 973 and 1428 K. They developed an expression for the overall rate coefficient of this reaction, of $k_{n\text{-butanol}+\text{OH}} = 4.118 \times 10^3 T^{2.944} \exp(1852/T)$ [cm³ mol⁻¹ s⁻¹]. The shock tube data are in good agreement with recent theoretical calculations performed by Zhou et al.,¹⁶ who used both CCSD(T)/cc-pVQZ//MP2/6-311g(d,p) and G3 methods to determine overall rate constant expressions for *n*-butanol + OH. Specifically, Zhou et al.¹⁶ determined an overall rate coefficient of $k_{n\text{-butanol}+\text{OH}} = 40.3 T^{3.57} \exp(2128/T)$ [cm³ mol⁻¹ s⁻¹] based on the G3 method. As seen in Figure 21, these overall rate constants of Vasu et al.¹⁵ and Zhou et al.¹⁶ are a factor of 2 higher than the rate constant used in the Black et al.¹ mechanism for the range of temperatures considered in the current work. For Figure 21, the data for the Black et al.¹ mechanism are the sum of the rate constants for H-atom abstraction by OH from the α , β , γ , and δ carbon sites and from the alcohol group of *n*-butanol.

Zhou et al.¹⁶ also determined temperature-dependent rate coefficients for the five product channels of the *n*-butanol + OH reaction. As seen in Figure 22, the branching fractions recommended by Zhou et al.¹⁶ (specifically focusing on the G3 calculations) differ from those adopted in the mechanism by Black et al.¹ In particular, the α channel (producing the $\text{C}_4\text{H}_8\text{OH-1}$ isomer) is much higher, and the β (producing the $\text{C}_4\text{H}_8\text{OH-2}$ isomer) and alcohol (producing the $\text{PC}_4\text{H}_8\text{OH}$ isomer) channels are much lower. In addition, the δ (producing the $\text{C}_4\text{H}_8\text{OH-4}$ isomer) channel has much stronger temperature dependence.

To quantify the effects of changing the overall rate coefficient and the branching fractions for the *n*-butanol + OH reaction, the recommendations from Zhou et al.¹⁶ (based on their G3 calculations) were substituted into the reaction mechanism by Black et al.¹ As expected based on the sensitivity analysis

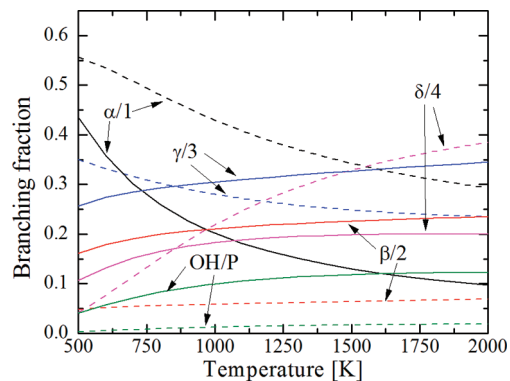


Figure 22. Branching fractions for the five H-atom abstraction channels by OH from the α , β , γ , and δ carbon sites and from the alcohol group of *n*-butanol. The legend includes the site of the H-atom abstraction and the designation of the corresponding $\text{C}_4\text{H}_8\text{OH}$ isomer produced. The solid lines are the values used in the Black et al.¹ mechanism, and the dashed lines are the values recommended by Zhou et al.¹⁶ based on their G3 calculations.

presented earlier, the modified reaction mechanism had a minor effect on the ignition delay time at $P = 3.25$ atm, $T = 975$ K, inert/ $\text{O}_2 = 5.64$, and *n*-butanol = 2.45%. Specifically, τ_{ign} increased from 18.6 to 21.8 ms. However, the modified reaction mechanism resulted in much higher endothermicity during the ignition delay period compared to the unmodified mechanism, with the temperature decreasing by 15 K (to 960 K) before ignition. The unmodified Black et al.¹ mechanism predicts weak endothermicity, with a decrease of only 0.5 K before ignition. There are also several significant changes in the intermediate species, and the model predictions from the modified reaction mechanism are presented as the dashed lines in Figure 12. Although there is an improvement in the prediction of CH_4 , C_2H_4 is significantly overproduced, with peak concentrations almost a factor of 3 higher than the unmodified Black et al.¹ mechanism. The modified mechanism dramatically improves the quantitative agreement between the model predictions for C_3H_6 and 1- C_4H_8 and the experimental data. $n\text{-C}_3\text{H}_7\text{CHO}$ concentrations are further underpredicted compared to the unmodified Black et al.¹ mechanism; however, the sum of the concentrations of the $\text{C}_4\text{H}_8\text{O}$ isomers predicted by the modified mechanism reproduces extremely well the measured values for $n\text{-C}_3\text{H}_7\text{CHO}$ concentrations, as is seen in Figure 12 with the green/short dashed line, marked *b*. The modified mechanism predicts the non-negligible amounts of these isomers for $t/\tau_{\text{ign}} < 0.4$. It is noted in Figure 12 with the green/short dashed line, marked *b*, that for CH_3CHO peak concentrations (off scale) of the sum of the $\text{C}_2\text{H}_4\text{O}$ isomers are around 1200 ppm, as compared to 3400 ppm for the unmodified mechanism.

The modified mechanism also changes the trend in *n*-butanol removal, where *n*-butanol is consumed almost linearly over the ignition delay time, rather than almost exponentially, as with the unmodified Black et al. mechanism. These changes are consistent with expectations based on the changes in the branching fractions and the reaction path analysis presented earlier. For example, decreasing the $\beta/\text{C}_4\text{H}_8\text{OH-2}$ and $\gamma/\text{C}_4\text{H}_8\text{OH-3}$ channels directly decreases the production of 1- C_4H_8 and C_3H_6 , respectively, while increasing the $\delta/\text{C}_4\text{H}_8\text{OH-4}$ channel increases a reaction path to form C_2H_4 . Overall, the performance of the reaction mechanism improved with the revisions to the *n*-butanol + OH reactions, with the key exceptions of $n\text{-C}_3\text{H}_7\text{CHO}$ and

C_2H_4 , which were not captured well quantitatively with either the modified or unmodified reaction mechanism.

4. CONCLUSIONS

The current work presents new experimental data on the ignition characteristics of *n*-butanol and species time histories of important intermediates formed during an ignition delay time of *n*-butanol. The experimental data are the first of their kind at the moderate temperatures (920–1040 K) and pressures (~ 3 atm) studied, and the data verify some expected trends, specifically Arrhenius behavior with no negative temperature dependence. Similar to hydrocarbons at comparable conditions, HO_2 and H_2O_2 kinetics dominate the reactivity of the *n*-butanol/air mixtures, and the data are in excellent agreement with model predictions based on recently developed reaction mechanisms for *n*-butanol. Further, the reaction mechanism by Black et al.¹ yields excellent quantitative agreement with experimental ignition data from the current work and previous shock tube studies over a broad range of temperatures (900–1800 K). Many of the reaction pathways important to predicting the intermediates are well represented in the chemical kinetic mechanism of Black et al.¹ A key exception identified in this study is C_2H_4 . The speciation data from the current study show high levels (100s of ppm and higher) of aldehydes (and related isomers), and alkenes are produced as intermediate species during *n*-butanol ignition. C_2H_4 and $n-C_3H_7CHO$ are expected to play a role in pollutant emissions, namely, soot and aldehydes; an understanding of their formation is essential for the successful implementation of *n*-butanol in the fuel infrastructure. Recent studies, like the important works by Vasu et al.¹⁵ and Zhou et al.¹⁶ on the overall reaction rate and specific branching channels of the *n*-butanol + OH reaction, have improved the understanding of the reaction pathways important to *n*-butanol combustion. However, more experimental and theoretical work is needed to improve the fidelity of our predictive understanding of *n*-butanol combustion chemistry.

■ ASSOCIATED CONTENT

5 Supporting Information. Figures representing the volume profile simulations of the UM RCF and tables of the experimental data are provided and can also be e-mailed upon request (contact Darshan M.A. Karwat at dippind@umich.edu). This material is available free of charge via the Internet at <http://pubs.acs.org>.

■ AUTHOR INFORMATION

Corresponding Author

*Fax: 734-647-3170. Phone: 734-763-7470. E-mail: dippind@umich.edu.

■ ACKNOWLEDGMENT

The authors would like to thank the U.S. Department of Energy Basic Energy Sciences, the U.S. Department of Energy via the University of Michigan Consortium on Efficient and Clean High-Pressure, Lean Burn (HPLB) Engines, the Michigan Memorial Phoenix Energy Institute, and the Graham Environmental Sustainability Institute for their financial support.

■ REFERENCES

- (1) Black, G.; Curran, H. J.; Pichon, S.; Simmie, J. M.; Zhukov, V. *Combust. Flame* **2010**, *157*, 363–373.
- (2) Gu, X.; Huang, Z.; Li, Q.; Tang, C. *Energy Fuels* **2009**, *23*, 4900–4907.
- (3) Jacobson, M. Z. *Environ. Sci. Technol.* **2007**, *41*, 4150–4157.
- (4) McEnally, C. S.; Pfefferle, L. D. *Proc. Combust. Inst.* **2005**, *30*, 1363–1370.
- (5) Veloo, P. S.; Wang, Y. L.; Egolfopoulos, F. N.; Westbrook, C. K. *Combust. Flame* **2010**, *157*, 1989–2004.
- (6) Osswald, P.; Güldenberg, H.; Kohse-Höinghaus, K.; Yang, B.; Yuan, T.; Qi, F. *Combust. Flame* **2011**, *158*, 2–15.
- (7) Grana, R.; Frassoldati, A.; Faravelli, T.; Niemann, U.; Ranzi, E.; Seiser, R.; Cattolica, R.; Seshadri, K. *Combust. Flame* **2010**, *157*, 2137–2154.
- (8) Moss, J. T.; Berkowitz, A. M.; Oehlschlaeger, M. A.; Biet, J.; Warth, V.; Glaude, P.; Battin-Leclerc, F. *J. Phys. Chem. A* **2008**, *112*, 10843–10855.
- (9) Liu, W.; Kelley, A. P.; Law, C. K. *Proc. Combust. Inst.* **2011**, *33*, 995–1002.
- (10) Heufer, K. A.; Fernandes, R. X.; Olivier, H.; Beeckmann, J.; Roehls, O.; Peters, N. *Proc. Combust. Inst.* **2011**, *33*, 359–366.
- (11) Noorani, K. E.; Akhi-Kumgeh, B.; Bergthorson, J. *Energy Fuels* **2010**, *24*, 5834–5843.
- (12) Sarathy, S. M.; Thomson, M. J.; Togbe, C.; Dagaut, P.; Halter, F.; Mounaim-Rousselle, C. *Combust. Flame* **2009**, *156*, 852–864.
- (13) Harper, M. R.; Van Geem, K. M.; Pyl, S. P.; Marin, G. B.; Green, W. H. *Combust. Flame* **2011**, *158*, 16–41.
- (14) Barnard, J. A. *Trans. Faraday Soc.* **1957**, *53*, 1423–1430.
- (15) Vasu, S. S.; Davidson, D. F.; Hanson, R. K.; Golden, D. M. *Chem. Phys. Lett.* **2010**, *497*, 26–29.
- (16) Zhou, C.-W.; Simmie, J. M.; Curran, H. J. *Combust. Flame* **2011** in press.
- (17) Dagaut, P.; Togbé, C. *Fuel* **2008**, *87*, 3313–3321.
- (18) Dagaut, P.; Togbe, C. *Energy Fuels* **2009**, *23*, 3527–3535.
- (19) Bourque, G.; Healy, D.; Curran, H.; Zinner, C.; Kalitan, D.; de Vries, J.; Aul, C.; Petersen, E. *ASME Conf. Proc.* **2008**, *2008*, 1051–1066.
- (20) Dagaut, P.; Sarathy, S. M.; Thomson, M. J. *Proc. Combust. Inst.* **2009**, *32*, 229–234.
- (21) He, X.; Donovan, M. T.; Zigler, B. T.; Palmer, T. R.; Walton, S. M.; Wooldridge, M. S.; Atreya, A. *Combust. Flame* **2005**, *142*, 266–275.
- (22) Walton, S. M.; He, X.; Zigler, B. T.; Wooldridge, M. S.; Atreya, A. *Combust. Flame* **2007**, *150*, 246–262.
- (23) Walton, S. M.; He, X.; Zigler, B. T.; Wooldridge, M. S. *Proc. Combust. Inst.* **2007**, *31*, 3147–3154.
- (24) Walton, S. M.; Wooldridge, M. S.; Westbrook, C. K. *Proc. Combust. Inst.* **2009**, *32*, 255–262.
- (25) He, X.; Zigler, B. T.; Walton, S. M.; Wooldridge, M. S.; Atreya, A. *Combust. Flame* **2006**, *145*, 552–570.
- (26) He, X.; Walton, S. M.; Zigler, B. T.; Wooldridge, M. S.; Atreya, A. *Int. J. Chem. Kinet.* **2007**, *39*, 498–517.
- (27) Walton, S. M.; Karwat, D. M.; Teini, P. D.; Gorny, A.; Wooldridge, M. S. *Fuel* **2011** in press.
- (28) Donovan, M. T.; He, X.; Zigler, B. T.; Palmer, T. R.; Wooldridge, M. S.; Atreya, A. *Combust. Flame* **2004**, *137*, 351–365.
- (29) Teini, P. D. *Ph.D. Thesis*, Univ. Mich. 2011
- (30) McBride, B. J.; Gordon, S.; Reno, M. A. *NASA Technical Memorandum 4513*, 1993.
- (31) Harper, M. R.; Van Geem, K. M.; Pyl, S. P.; Marin, G. B.; Green, W. H. *Combust. Flame* **2011**, *158*, 16–41.